

Influence of Kuroshio Extension Variability on the North Pacific Atmosphere and Pacific Decadal Precession

E. Nishchitha S Silva (✉ netige@bu.edu)

Boston University <https://orcid.org/0000-0002-8543-2245>

Bruce T Anderson

Boston University

Research Article

Keywords: Kuroshio Current System, North Pacific Climate, Ocean-Atmosphere Interactions, Pacific Decadal Precession, Decadal Climate Variability, mesoscale and large-scale ocean currents

Posted Date: March 21st, 2022

DOI: <https://doi.org/10.21203/rs.3.rs-1451566/v1>

License:  This work is licensed under a Creative Commons Attribution 4.0 International License.

[Read Full License](#)

1 **Influence of Kuroshio Extension Variability on the North Pacific Atmosphere and**
2 **Pacific Decadal Precession**

3 **E. Nishchitha S. Silva¹ and Bruce T. Anderson¹**

4 ¹Department of Earth and Environment, Boston University, Boston, MA, USA

5

6 Corresponding author: E. Nishchitha S. Silva (netige@bu.edu)

7

8

9

10

11

12

13

14

15

16

17

18

19

20

21 **Acknowledgments**

22 We acknowledge the multiple institutions that provided data for this study. High-resolution sea
23 surface temperature data were provided by GHRSSST, Met Office, and CMEMS.
24 NOAA_ERSST_V3b data provided by the NOAA/OAR/ESRL PSL, Boulder, Colorado, USA, from
25 their Web site. ERA5 monthly mean data on single levels from 1979 to the present was
26 provided by the Climate Data Store of the European Centre for Medium-Range Weather
27 Forecast (ECMWF) Copernicus Services. NCEP/NCAR Reanalysis 1 data were provided by the
28 National Centers for Environmental Prediction/National Weather Service/NOAA/U.S.
29 Department of Commerce.

30 **Abstract**

31 Recent research has revealed links between a quasi decadal mode of climate variability over the
32 North Pacific – the Pacific Decadal Precession (PDP) – and the North Pacific’s western boundary
33 currents extension – the Kuroshio Extension (KE). It is suggested that on decadal time scales the
34 PDP both responds to and influences the KE variability. A question yet to be answered is
35 whether it is the large-scale or the mesoscale variations of the KE region that influence the
36 overlying and downstream atmosphere and hence the PDP evolution. Using high-resolution sea
37 surface temperature data (1981-2018) from the global ocean Operational Sea Surface
38 Temperature (SST) and Sea Ice Analysis, low resolution Extended Reconstructed SST (ERSST)
39 version 3b data (1949-2018), geopotential height data from the European Centre for Medium-
40 Range Weather Forecasts (ECMWF) and the National Centers for Environmental Prediction we
41 find that it is the large-scale variations in the KE region that correlate best with the overlying
42 and downstream atmosphere instead of the mesoscale variations. In particular, the second
43 mode of the large-scale KE region, which is characterized by warming (cooling) of the ocean
44 south (north) of the KE, sets up a PDP-like north-south atmospheric pressure dipole over the
45 North Pacific Ocean by altering the large-scale baroclinicity of the atmosphere. In turn, this
46 enhances the overlying storm track, resulting in a downstream response over the North
47 American continent and the formation of a subsequent east-west pressure dipole. As a result,
48 there is a strong correlation between large-scale variations in the KE region and the evolution of
49 the PDP over the next three years.

50

51 **Keywords:** Kuroshio Current System, North Pacific Climate, Ocean-Atmosphere Interactions,
52 Pacific Decadal Precession, Decadal Climate Variability, mesoscale and large-scale ocean
53 currents

54

55

56

57 **Statements and Declarations**

58 **Conflicts of interest/Competing interests** Not applicable

59 **Data Availability:** The data that support the findings of this study are available from:

- 60 1. <https://resources.marine.copernicus.eu/products> (Operational Sea Surface
61 Temperature and Sea Ice Analysis)
- 62 2. <https://psl.noaa.gov/data/gridded/data.noaa.ersst.v3.html> (National Oceanic and
63 Atmospheric Administration (NOAA) Extended Reconstructed SST (ERSST) version 3b
64 data)
- 65 3. <https://cds.climate.copernicus.eu/> (ERA5 monthly averaged data)
- 66 4. <https://psl.noaa.gov/data/gridded/data.ncep.reanalysis.html> (NCEP/NCAR Reanalysis 1)

67
68 **Code availability:** The code is available from the corresponding author.

69

70

71

72

73

74

75

76

77

78

79

80 1. Introduction

81 Western boundary currents and their eastward extensions play a fundamental role in shaping
82 the climates by influencing ocean-atmosphere interactions and modulating sea surface
83 temperature (SST) variations (Kwon et al., 2010; Omrani et al., 2019). Among these currents,
84 the Kuroshio Extension (KE), the eastward extension of the North Pacific subtropical gyre's
85 western boundary current (Kuroshio Current) contributes to the ocean-atmosphere interactions
86 in the North Pacific Ocean (Qiu, 2003). Further, the characteristic decadal variations in both SST
87 and sea surface height (SSH) of the KE are influenced by the propagation of Rossby waves
88 resulting from anomalous Ekman pumping in the central North Pacific (Nonaka et al., 2006).
89 Such decadal variations of the Kuroshio Current have been linked to well-known decadal
90 atmospheric variations. Indeed, it has been revealed that the Pacific Decadal Oscillation (PDO)
91 evolution is strongly correlated with the vertically integrated transport of the Kuroshio Current
92 (Andres et al., 2009) on decadal timescales, which in turn can modify the strength of the
93 overlying Aleutian low anomalies and El Nino-Southern Oscillation events (ENSO) (Schneider &
94 Cornuelle, 2005).

95 Recently, though, a new mode of quasi-decadal atmospheric variability over the North Pacific
96 has been discovered and termed as the Pacific Decadal Precession (PDP) (Anderson et al.,
97 2016). The PDP is characterized by a counterclockwise progression of an atmospheric pressure
98 dipole centered on the mid-latitude North Pacific. It comprises a north-south teleconnection
99 phase (N-S phase) which maps onto the North Pacific Oscillation (NPO) and an east-west
100 teleconnection phase (E-W phase) which maps onto the Circumglobal Teleconnection Pattern
101 (CTP). These two modes of PDP variability have been linked to regional and hemispheric scale
102 climate variations that include extended droughts in the Northwest United States, abnormal
103 warmth of the Western United States, and cold air outbreaks in the eastern United States
104 (Anderson et al., 2016, 2017; Harnik et al., 2016; Singh et al., 2016; Stevenson et al., 2015).
105 Further, the evolution of PDP has direct impacts on the marine environment. For instance,
106 during the N-S phase of the PDP large-scale negative sea surface temperature (SST) anomalies
107 are present over the central equatorial Pacific while a warming signal can be seen along the
108 east coast of North America. With regards to the E-W phase, a warming signal occurs first in the

109 eastern Pacific that then extends along the west coast of North America in subsequent years.
110 This PDP-related SST evolution in fact coincides with both the 2012 marine heatwave over the
111 Northeast U.S. continental shelf (Mills et al., 2013) and the 2014-2015 heatwaves along the
112 West Coast of the United States (Lorenzo & Mantua, 2016).

113 Given the fact that both PDP and KE have a quasi-decadal periodicity in their variations,
114 Anderson (2019) investigated potential links between the PDP and KE employing empirical
115 methods. That study revealed that links between KE and PDP exist and that the PDP both forces
116 and responds to KE variability on these decadal timescales. The same study further suggested a
117 presence of a self-sustaining decadal oscillation of the ocean-atmosphere system across the
118 extratropical North Pacific where large-scale ocean-atmosphere coupling positively reinforces
119 atmospheric circulations that generate KE variability while mesoscale ocean-atmosphere
120 coupling allows the subsequent KE variability to reverse these atmospheric circulations. Given
121 the above findings, our present investigation is motivated by the need to methodically
122 investigate the linkages between the PDP and the KE.

123 When investigating the coupling between ocean and atmosphere, a longstanding question
124 remains as to whether it is the largescale variations (Joyce et al., 2009; Qiu, 2002) or mesoscale
125 variations (Byrne et al., 2015; Chelton & Xie, 2010; Hogg et al., 2009; Siqueira et al., 2021) of
126 the ocean that significantly forces the overlying and downstream atmosphere. For instance,
127 through observational studies (Frankignoul & Sennéchaël, 2007; Gan & Wu, 2013; Q. Liu et al.,
128 2006; Taguchi et al., 2012; Wen et al., 2010) and modeling studies (Gan & Wu, 2012; Z. Liu &
129 Wu, 2004; Smirnov et al., 2015) it has been argued that the KE and Oyashio Extension regions
130 generate atmospheric responses primarily by modifying the overlying transient eddy feedbacks
131 that can amplify the downstream response. Further O'Reilly & Czaja (2015) reported that as a
132 response to the interannual variability of the KE front the Pacific storm track exhibits zonal
133 shifts. However, all of these studies look into coarse resolution data and models and did not
134 look into the mesoscale SST variations in particular. By contrast, Sugimoto & Hanawa (2011)
135 reported that mesoscale SST variations are primarily responsible for the turbulent heat flux
136 variations in the Kuroshio Oyashio Confluence Region (KOCR) region. Further, they indicated
137 that these SST anomalies in the KOCR are formed through warm ocean eddies detached from

138 the KE. Since then, several analyses have focused on mesoscale SST variations in the KE and
139 their influence on the atmosphere (Jing et al., 2019; Kawai et al., 2014; Ma et al., 2015;
140 Putrasahan et al., 2013; Siqueira et al., 2021; Zhang et al., 2019). Of these works, Ma et al.
141 (2015) reported that mesoscale SST variability confined in the KOCR region exerts a significant
142 distant influence on winter rainfall variability along the Northern Pacific coast of the United
143 States. Siqueira et al. (2021) also indicated that KE variability affects rainfall variability along the
144 same region and reveals the need to use models that resolve mesoscale ocean eddies in order
145 to capture these interactions.

146 Taking all these findings into consideration our work is designed to look at which scale of KE SST
147 variations links with the evolution of PDP. This paper reports the results of our analysis
148 conducted to answer the following questions: 1) What scale of KE variations induces the PDP
149 like atmospheric structure over the North Pacific Ocean; 2) what is the downstream
150 atmospheric response to KE variations, and; 3) what is the causal link between this ocean-
151 atmosphere link? The outline of the paper is as follows. Section 2 briefly describes the data
152 used in the study and methods we employed to quantify different scales of KE variations and
153 links between these variations and atmospheric circulations. In section 3, we show the results
154 of our analysis of empirical links between KE variations and the downstream atmosphere.
155 Section 4 discusses and summarizes our findings.

156 **2. Data and Methods**

157 **2.1. Data**

158 For this study, we used multiple sets of SST and atmospheric datasets. High-resolution SST data
159 come from the global ocean Operational Sea Surface Temperature and Sea Ice Analysis (OSTIA)
160 SST reprocessed dataset (Good et al., 2020) which was obtained from European Union
161 Copernicus Marine Services data portal. The OSTIA global SST reprocessed product provides
162 daily mean values of SST at a 0.05 x 0.05 horizontal spatial resolution spanning from the year
163 1981 to the present. In addition, we used the National Oceanic and Atmospheric Administration
164 (NOAA) Extended Reconstructed SST (ERSST) version 3b data (Smith et al., 2008; Y. Xue et al.,
165 2003) obtained from the website of NOAA Physical Science Laboratory, Boulder, Colorado, USA.

166 NOAA ERSST v3b has a global spatial coverage at a spatial resolution of 2 x 2 degrees. It
167 provides monthly SST values from 1854 to the present.

168 We also used the European Centre for Medium-Range Weather Forecasts fifth-generation
169 reanalysis ERA5 (Hersbach et al., 2019) high-resolution atmospheric data in conjunction with
170 the OSTIA SST data. Geopotential height data were obtained from ERA5 which is available via
171 the data portal of Copernicus Atmosphere Monitoring Service. This data has a monthly
172 temporal resolution and temporal coverage of 1979 to present at a 0.25 x 0.25 spatial
173 resolution. The vertical coverage is from 1000hPa to 1hPa with a vertical resolution of 37
174 pressure levels. In addition, we use low-resolution NCEP/NCAR Reanalysis 1 data (Kalnay et al.,
175 1996) available from the National Centers for Environmental Prediction (NCEP) jointly with
176 National Center for Atmospheric Research (NCAR). Data are available as 4-times a day, daily,
177 and monthly values from 1948 to present at a spatial resolution of 2.5 x 2.5. The vertical
178 coverage is from 1000hPa to 10hPa with a vertical resolution of 17 pressure levels.

179 For both atmospheric and ocean analysis, we confined the monthly values from November to
180 April of the subsequent year. This is the period of the year that the PDP is most active and also
181 corresponds to when the ocean/atmosphere coupling is strongest (Ferreira & Frankignoul,
182 2005; Kwon et al., 2010; O'Reilly & Czaja, 2015; Qiu et al., 2007). Anomalies were derived by
183 removing the climatological mean of each month from the monthly values for that month.

184 **2.2. Methods**

185 **2.2.1. Separating MS and LS SSTs.**

186 To develop mesoscale (MS) and largescale (LS) indices for the KE region we used Copernicus
187 high-resolution SST data. To separate MS SSTA signals from LS SSTAs we used a 5° x 5° spatial
188 boxcar filter following the studies of Itoh & Yasuda (2010); Putrasahan et al. (2013); Zhang et al.
189 (2019). Figure 1a shows the raw SSTAs in the North Pacific where we see high variability within
190 the KOCR. Figure 1b shows low-pass filtered SSTAs (L-SSTAs) and figure 1c shows the high-pass
191 filtered (M-SSTAs) in the North Pacific. It is evident that the filter we use is able to separate the
192 largescale and mesoscale SSTAs effectively based on the rationale that the mesoscale eddies
193 have diameters smaller than 5° in general.

194 **2.2.2. Determining the domain for KE.**

195 To determine the domain area for the KE region and KOCR region we looked into the maximum
196 variance of SSTAs during the wintertime spanning 1981 to 2018. Also, we considered the KE
197 domain used by previous studies (Qiu et al., 2014) which is 31°–36° N, 140°–165° E and the
198 KOCR region used in the (Anderson, 2019) investigations which is 35°–42° N, 140°–172.5° E. For
199 the purposes of our study, we decided on the KE region domain by overlapping the above two
200 domains with the region of high variance SST (30°–42° N, 140°–172° E). Hereafter we refer to
201 this domain as the KE region. The domain is marked in figure 1 maps as a black rectangle.

202 **2.2.3. Developing a KE index for both LS and MS.**

203 To quantitatively measure the KE variation, we developed multiple indices. Since our objective
204 is to look into the influence of both mesoscale and largescale variations in the KE region on the
205 overlying and downstream atmosphere we developed both mesoscale and largescale indices.
206 To create the mesoscale index, we first applied a similar method developed by (Zhang et al.,
207 2019). Once the monthly mean SST (T) anomaly was separated into its mesoscale SST
208 component (T*) and largescale SST component, the magnitude of the MAAST anomaly (Vi) was
209 calculated by (T*T*)^{1/2}. Then we calculated the spatial summation of Vi for each month ([Vi]).
210 The square brackets indicate spatial summation. Then we calculated the month-to-month
211 standard deviation [Vi], defined here as (S). From this, we calculated and Mesoscale index
212 values (Mi) for each cold season month from 1981 to 2018 using,

213
$$M_i = \frac{[V_i] - [\bar{V}]}{S} \text{ --- Equation 1}$$

214 We call this index MS KI. For comparison, we also conducted an Empirical Orthogonal Function
215 (EOF) analysis on M-SSTAs. This EOF analysis provided the leading mode of mesoscale SST
216 variability in the KE region. The time series of the leading EOF of M-SSTA eigenvalues (EOF1)
217 was obtained and hereafter referred to as MS EOF 1. To represent large-scale variations of L-
218 SSTAs in the KE region we used EOF analysis. Here we used the 1st and 2nd EOF eigenvectors (LS
219 EOF1 and LS EOF2 respectively) as the two largescale indices. The explained variance of LS EOF1
220 (LS EOF2) was 58% (20%).

248 vector autoregression (VAR) that tests the two-way interaction between SST anomalies and the
 249 detrended monopole index. This is given by equation 3:

$$250 \quad MPI_t = \alpha_1 + \sum_{i=l}^s \beta_{1i} MPI_{t-i} + \sum_{i=1}^s \gamma_{1i} SST_{t-i} + e_{1t} \text{ --- --- --- Equation 3,}$$

251 where α , β , and γ are regression coefficients, e is the error term, and s is the lag length.
 252 Equations 3 is developed based on VAR where current values of MPI and SST are a function of
 253 lagged MPI and SST values. In our analysis, we looked at how early winter SSTs lead to the
 254 development of the monopole over North America in the late winter. Therefore, our lag length
 255 is one while our current values are late winter mean values (Jan-Feb) and lagged values (t-i) are
 256 early winter (Nov-Dec) mean values. The direction of the causal order was determined using a
 257 restricted version of equation 4, in which the causal variable is eliminated by restricting γ to
 258 zero. Then the restricted versions of equation 3 becomes equation 4:

$$260 \quad MPI_t = \alpha_1 + \sum_{i=l}^s \beta_{1i} MPI_{t-i} + e_{1t} \text{ --- --- --- Equation 4}$$

261 To test whether the restricted estimates are statistically different from unrestricted estimates
 262 we calculated a test statistic ω using equation 5:

$$263 \quad \omega = \frac{(RSS_r - RSS_u)/s}{RSS_u/(T - k)} \text{ --- --- --- Equation 5,}$$

264 where RSS is the sum of residual squares, where r and u subscripts pertain to restricted and
 265 unrestricted values respectively. T is the number of observations, k is the number of regressors
 266 in the unrestricted version of the equation, and s is the number of coefficients restricted to zero
 267 in equation 3. For our analysis s = 1 since we investigated the causal effect of SSTs on MPI from
 268 early winter to late winter. We evaluated the test statistic using an F distribution to evaluate
 269 the null hypothesis "SST does not cause variability in the downstream MPI" at a 95%
 270 significance level. A statistically significant increment in RSS_r relative to RSS_u indicates that early

271 winter values of SSTs have information about the late winter values of MPI, as quantified by ω .
272 This analysis was conducted on every SST grid-point within our SST domain.

273 **3. Results**

274 **3.1. Influence of Large-scale and Mesoscale KE Region Variations**

275 Figure 2 presents the various KE indices developed to represent the mesoscale (a-b) and large-
276 scale (c-d) KE variability. These four indices consist of a mesoscale index produced using
277 equation 1 (MS KI – Figure 2a), the leading EOF of mesoscale SSTAs (MS EOF1 – Figure 2b), the
278 leading EOF of largescale SSTAs (LS EOF 1 – Figure 2c), and the second EOF of largescale SSTAs
279 (LS EOF2 – Figure 2d). Examining the basin-scale SST pattern corresponding to mesoscale
280 variations of the KE region (Figures 3a & 3b), we find these are substantially weaker compared
281 with basin-scale SST anomalies associated with the large-scale KE variations. In particular, the
282 leading mode of large-scale KE variability is characterized by a warm tongue of water extending
283 from the west to the east, while cooler conditions prevail in the eastern North Pacific (Figure
284 3c). By contrast, the 2nd mode of large-scale KE variability is characterized by warmer
285 temperatures to the south and cooler temperatures to the north of the KE region, which in this
286 phase tends to enhance the climatological meridional temperature gradient across the North
287 Pacific Ocean (Figure 3d).

288 The response of the overlying atmosphere to the KE region variations is included in figure 4.
289 These results suggest that again it is the large-scale variations in the KE region that have a
290 greater influence on the 850hPa GPH variations above the North Pacific Ocean. We do not
291 observe a significant influence of the KE's mesoscale variations on the overlying atmosphere
292 (Figures 4a & 4b). By contrast, the 850hPa GPH anomaly response to LS EOF 1 indicates a high-
293 pressure monopole over the North Pacific Ocean (Figure 4c). The response to LS EOF 2 is the
294 formation of a north-south dipole pressure pattern over the North Pacific Ocean, which is
295 similar to the N-S phase of the PDP. At the same time, the 850hPa atmosphere downstream of
296 KE (over the North American continent) indicates a high-pressure system associated with the LS
297 EOF 2 (Figure 4d). Thus, this analysis suggests that neither the mesoscale KE variations nor the
298 leading mode of large-scale variations in the KE region itself correspond with a PDP-like dipole

299 pressure pattern over the North Pacific Ocean. Instead, it is the meridional structure of the 2nd
300 leading mode of large-scale variation of KE region that corresponds with PDP's N-S phase. To
301 confirm the result that large-scale variations of the KE region more strongly influence the
302 atmosphere, we employ the coarse resolution longer duration NOAA ERSST version 3b dataset
303 from 1948 to 2018 to recreate the LS EOF 2. Figure 5a shows a comparison between short-term
304 and long-term LS EOF 2 indices. When the extended LS EOF 2 is regressed over the SSTs and
305 850hPa GPHs both parameters show a similar structure to ones related to the short-term LS
306 EOF 2 (Figures 5b & 5c). Hence for the next analyses, we will continue to use the coarser-
307 resolution but longer duration data available from the NOAA reanalysis products.

308 **3.2. Coupled Link between the Ocean and the Atmosphere**

309 To determine the coupled link between KE region variations and the overlying and downstream
310 atmosphere we examined the response of multiple atmospheric variables to the KE variations
311 (Figure 6). First, we note that the atmospheric structure over the North Pacific is equivalent
312 barotropic with a same-signed geopotential height dipole found aloft (300hPa) as in the lower
313 troposphere (850hPa). In addition, though there is a very substantial change in downstream,
314 upper-tropospheric geopotential heights situated over North America. Given the upper-
315 tropospheric dipole pressure pattern over the North Pacific, the response of the 300hPa
316 wintertime storm track ($v'v'$) intensifies downstream of the KE region (Figure 6c) consistent
317 with the enhanced baroclinity induced by the KE's large-scale meridional temperature gradient.
318 As a result of the enhanced storm track there is a reduction in northward atmospheric heat
319 transport over the North Pacific Ocean, which serves to sustain the low-pressure anomalies to
320 the north (Figure 6d). To understand the downstream response, particularly over North
321 America, we next examine the 300hPa zonal flux of meridional momentum ($u'v'$) (figure 6e).
322 The response of $u'v'$ to the KE variability indicates that over the North Pacific the anomalous
323 $u'v'$ fields tend to enhance the climatological values, consistent with an enhancement of zonal
324 momentum, i.e. an intensification and extension of the storm track. However over North
325 America, we find that the anomalous values tend to offset the climatological values, and in
326 particular the large-scale convergence of zonal momentum that sustains the jet in the region.
327 This is confirmed by looking at the divergence of the E-vectors (Figure 6f) which indicates a

328 strengthening of the jet stream over the North Pacific resulting from the convergence of zonal
329 momentum by baroclinic eddies. However, over North America, there is convergence of the E-
330 vectors, which tends to reduce the zonal momentum. At the same time to the north, there is a
331 divergence of the E-vector field. While typically associated with an enhancement of the zonal
332 momentum field, it also represents the divergence of relative vorticity, which in turn is
333 consistent with the downstream formation of upper tropospheric high-pressure anomalies in
334 these regions discussed earlier.

335 **3.3 Causal Effect of KE on Downstream Atmosphere**

336 We next analyzed how early winter SSTs at each grid point in our domain Granger cause the
337 late winter monopole index downstream (black box domain over North America in figure 6b).
338 Figure 7 shows the results obtained when November and December months are considered as
339 early winter and the January February months are considered as late winter. Figure 7 identifies
340 that early winter SSTs falling within our KE domain Granger causes the late winter monopole
341 index. This pattern of SSTs falls within the southern portion of the domain indicating that only
342 half of the KE domain's SSTs are informative. Also, the pattern mimics the jet structure of KE.
343 The same result holds for when early winter is considered as November to December and late
344 winter is considered January through March (not shown). Further, the result holds if we
345 consider only the month of December as a precursor to January and February (not shown).

346 **4. Discussion and Summary**

347 Decadal variations in the KE (Qiu et al., 2014; Qiu & Chen, 2005; Taguchi et al., 2007) have been
348 empirically linked with the evolution of a recently discovered Pacific Decadal Precession (PDP) a
349 quasi-decadal atmospheric variability occur over the North Pacific Ocean (Anderson et al., 2016,
350 2017). In this paper, we investigated how variations in the KE region augment downstream SST
351 and atmospheric responses that align with the evolution of the PDP. The major question we
352 addressed is whether it is the largescale or mesoscale variations of the KE region that
353 determined the PDP-like response in the atmosphere.

354 The analysis we conducted indicated that it is neither the leading modes of mesoscale nor
355 large-scale KE variations that produce a PDP-like dipole structure over the North Pacific Ocean.

356 Instead, it is the 2nd mode of large-scale SST variability related to a large-scale meridional
357 gradient of sea surface temperatures across the North Pacific that coincides with the N-S phase
358 of the PDP. At the same time, we observed a downstream response in the upper atmosphere
359 (300hPa GPH) that further aligns with the onset of the E-W phase of the PDP. Further analysis
360 of extended oceanic and atmospheric data indicates that the mechanism by which the KE
361 augments the overlying PDP-like dipole and the downstream high-pressure center is the
362 following. The influence of large-scale KE variations sets up a meridional temperature gradient
363 over the North Pacific Ocean. This meridional SST pattern is similar to the 2nd mode of SST
364 variations in the North Pacific Ocean shown by Furtado et al. (2011). The warming (cooling) to
365 the south (north) sets up a high (low) pressure center to the south (north). This happens
366 because of the atmosphere's barotropic response to turbulent heat fluxes from ocean
367 temperature anomalies in the extratropics (Ferreira & Frankignoul, 2005; Frankignoul, 1985;
368 Kushnir et al., 2002; Lau & Nath, 1990; Namias & Cayan, 1981; Shutts, 1987). These fluxes
369 modify the atmospheric baroclinicity and the overlying storm track as well as transient eddy
370 activity, and vorticity flux convergence which sustains the atmospheric modifications (Fang &
371 Yang, 2016; Kushnir et al., 2002; Lau & Nath, 1990; J. Xue et al., 2018; Zhou et al., 2017).
372 Further, due to the altered meridional temperature gradient in the Pacific Ocean and the
373 overlying atmosphere, downstream baroclinicity is also modified. In the case of high pressure to
374 the south and low pressure to the north the storm track strengthens downstream and at the
375 same time diminishes the meridional heat transport (J. Xue et al., 2018). The intensification of
376 the storm track to the east of the KE region is not present over the North American continent,
377 however. Instead, we see a weakening of storm track along the same latitudinal region and a
378 shift to the north. This results in a strengthened westerly flow to the north and a weakened
379 westerly flow to the south. The development of the accompanying upper-tropospheric high-
380 pressure anomaly is supported by the divergence of relative vorticity, as captured by the
381 divergence of E-vectors (Hoskins et al., 1983). To confirm these results, we conducted a Granger
382 causality analysis to provide further empirical evidence that the KE causes downstream
383 atmospheric modifications related to the PDP. Indeed results indicated that the formation of

384 the downstream high-pressure pattern over North American continent is caused by SSTs within
385 the KE region.

386 Returning to our original motivation for this research, according to Anderson (2019) the PDP
387 both forces and responds to KE variability on decadal timescales through the presence of a self-
388 sustaining decadal oscillation of the ocean-atmosphere system across the extratropical North
389 Pacific in which large-scale ocean-atmosphere coupling positively reinforces atmospheric
390 circulation that generates KE variability while mesoscale ocean-atmosphere coupling allows the
391 subsequent KE variability to reverse these atmospheric circulations. This coupled mode of
392 variability was termed the named Ebian Pacific Precession (EPP) and comprised three stages:
393 1) a teleconnection stage where KE heat flux anomalies induce teleconnected atmospheric
394 pressure anomalies; 2) a tethered stage during which SST anomalies and atmospheric pressure
395 anomalies intensify westward migration of the dipole, and; 3) a tunneling stage where wind
396 stress forcing generates a westward propagating Rossby wave that subsequently modifies the
397 KE structure giving rise to the opposite sign of the teleconnection stage. Our major analysis in
398 this paper investigated the teleconnection stage, with a particular focus on what scale of KE
399 variations energizes this stage. Given our findings, it is not surprising that a lead-lag correlation
400 analysis between the KE index and PDP indicates a significant correlation between the KE index
401 and the PDP's E-W phase at a 3-year lead time (Figure 8), highlighting that the large-scale KE
402 variations can influence the subsequent evolution of the PDP. That said, future investigations
403 have to be conducted to determine the dynamics of both the tethered and tunneling stages in
404 the EPP chain.

405

406

407

408

409

410

411 **References**

- 412 Anderson, B. T. (2019). Empirical Evidence Linking the Pacific Decadal Precession to Kuroshio
413 Extension Variability. *Journal of Geophysical Research: Atmospheres*, 124(23), 12845–12863.
414 <https://doi.org/10.1029/2019JD031163>
- 415 Anderson, B. T., Furtado, J. C., Lorenzo, E. D., & Gianotti, D. J. S. (2017). Tracking the Pacific
416 Decadal Precession. *Journal of Geophysical Research: Atmospheres*, 122(6), 3214–3227.
417 <https://doi.org/10.1002/2016JD025962>
- 418 Anderson, B. T., Gianotti, D. J. S., Furtado, J. C., & Lorenzo, E. D. (2016). A decadal precession of
419 atmospheric pressures over the North Pacific. *Geophysical Research Letters*, 43(8), 3921–3927.
420 <https://doi.org/10.1002/2016GL068206>
- 421 Byrne, D., Papritz, L., Frenger, I., Münnich, M., & Gruber, N. (2015). Atmospheric Response to
422 Mesoscale Sea Surface Temperature Anomalies: Assessment of Mechanisms and Coupling
423 Strength in a High-Resolution Coupled Model over the South Atlantic. *Journal of the*
424 *Atmospheric Sciences*, 72(5), 1872–1890. <https://doi.org/10.1175/JAS-D-14-0195.1>
- 425 Chelton, D. B., & Xie, S.-P. (2010). Coupled ocean-atmosphere interaction at oceanic
426 mesoscales. *Oceanography*, 23(4), 52–69.
- 427 Fang, J., & Yang, X.-Q. (2016). Structure and dynamics of decadal anomalies in the wintertime
428 midlatitude North Pacific ocean–atmosphere system. *Climate Dynamics*, 47(5–6), 1989–2007.
429 <https://doi.org/10.1007/s00382-015-2946-x>
- 430 Ferreira, D., & Frankignoul, C. (2005). The Transient Atmospheric Response to Midlatitude SST
431 Anomalies. *Journal of Climate*, 18(7), 1049–1067. <https://doi.org/10.1175/JCLI-3313.1>
- 432 Frankignoul, C. (1985). Sea surface temperature anomalies, planetary waves, and air-sea
433 feedback in the middle latitudes. *Reviews of Geophysics*, 23(4), 357–390.
- 434 Frankignoul, C., & Sennéchaël, N. (2007). Observed influence of North Pacific SST anomalies on
435 the atmospheric circulation. *Journal of Climate*, 20(3), 592–606.
- 436 Furtado, J. C., Lorenzo, E. D., Schneider, N., & Bond, N. A. (2011). North Pacific decadal
437 variability and climate change in the IPCC AR4 models. *Journal of Climate*, 24(12), 3049–3067.
- 438 Gan, B., & Wu, L. (2012). Modulation of atmospheric response to North Pacific SST anomalies
439 under global warming: A statistical assessment. *Journal of Climate*, 25(19), 6554–6566.
- 440 Gan, B., & Wu, L. (2013). Seasonal and long-term coupling between wintertime storm tracks
441 and sea surface temperature in the North Pacific. *Journal of Climate*, 26(16), 6123–6136.
- 442 Good, S., Fiedler, E., Mao, C., Martin, M. J., Maycock, A., Reid, R., Roberts-Jones, J., Searle, T.,
443 Waters, J., & While, J. (2020). The current configuration of the OSTIA system for operational

444 production of foundation sea surface temperature and ice concentration analyses. *Remote*
445 *Sensing*, 12(4), 720.

446 Granger, C. W. (1969). Investigating causal relations by econometric models and cross-spectral
447 methods. *Econometrica: Journal of the Econometric Society, Journal Article*, 424–438.

448 Harnik, N., Messori, G., Caballero, R., & Feldstein, S. B. (2016). The Circumglobal North
449 American wave pattern and its relation to cold events in eastern North America. *Geophysical*
450 *Research Letters*, 43(20), 11,015–11,023. <https://doi.org/10.1002/2016GL070760>

451 Hersbach, H., Bell, B., Berrisford, P., Biavati, G., Horányi, A., Sabater, J. M., Nicolas, J., Peubey,
452 C., Radu, R., & Rozum, I. (2019). ERA5 monthly averaged data on single levels from 1979 to
453 present. [https://cds.climate.copernicus.eu/cdsapp#!/dataset/reanalysis-era5-single-levels-](https://cds.climate.copernicus.eu/cdsapp#!/dataset/reanalysis-era5-single-levels-monthly-means?tab=overview)
454 [monthly-means?tab=overview](https://cds.climate.copernicus.eu/cdsapp#!/dataset/reanalysis-era5-single-levels-monthly-means?tab=overview)

455 Hogg, A. M. C., Dewar, W. K., Berloff, P., Kravtsov, S., & Hutchinson, D. K. (2009). The Effects of
456 Mesoscale Ocean–Atmosphere Coupling on the Large-Scale Ocean Circulation. *Journal of*
457 *Climate*, 22(15), 4066–4082. <https://doi.org/10.1175/2009JCLI2629.1>

458 Hoskins, B. J., James, I. N., & White, G. H. (1983). The shape, propagation and mean-flow
459 interaction of large-scale weather systems. *Journal of Atmospheric Sciences*, 40(7), 1595–1612.

460 Itoh, S., & Yasuda, I. (2010). Characteristics of Mesoscale Eddies in the Kuroshio–Oyashio
461 Extension Region Detected from the Distribution of the Sea Surface Height Anomaly. *Journal of*
462 *Physical Oceanography*, 40(5), 1018–1034. <https://doi.org/10.1175/2009JPO4265.1>

463 Jing, Z., Chang, P., Shan, X., Wang, S., Wu, L., & Kurian, J. (2019). Mesoscale SST dynamics in the
464 Kuroshio–Oyashio extension region. *Journal of Physical Oceanography*, 49(5), 1339–1352.

465 Joyce, T. M., Kwon, Y.-O., & Yu, L. (2009). On the relationship between synoptic wintertime
466 atmospheric variability and path shifts in the Gulf Stream and the Kuroshio Extension. *Journal of*
467 *Climate*, 22(12), 3177–3192.

468 Kalnay, E., Kanamitsu, M., Kistler, R., Collins, W., Deaven, D., Gandin, L., Iredell, M., Saha, S.,
469 White, G., & Woollen, J. (1996). The NCEP/NCAR 40-year reanalysis project. *Bulletin of the*
470 *American Meteorological Society*, 77(3), 437–472.

471 Kawai, Y., Tomita, H., Cronin, M. F., & Bond, N. A. (2014). Atmospheric pressure response to
472 mesoscale sea surface temperature variations in the Kuroshio Extension region: In situ
473 evidence. *Journal of Geophysical Research: Atmospheres*, 119(13), 8015–8031.

474 Kushnir, Y., Robinson, W. A., Bladé, I., Hall, N. M. J., Peng, S., & Sutton, R. (2002). Atmospheric
475 GCM response to extratropical SST anomalies: Synthesis and evaluation. *Journal of Climate*,
476 15(16), 2233–2256.

477 Kwon, Y.-O., Alexander, M. A., Bond, N. A., Frankignoul, C., Nakamura, H., Qiu, B., & Thompson,
478 L. A. (2010). Role of the Gulf Stream and Kuroshio–Oyashio Systems in Large-Scale
479 Atmosphere–Ocean Interaction: A Review. *Journal of Climate*, 23(12), 3249–3281.
480 <https://doi.org/10.1175/2010JCLI3343.1>

481 Lau, N.-C., & Nath, M. J. (1990). A general circulation model study of the atmospheric response
482 to extratropical SST anomalies observed in 1950–79. *Journal of Climate*, 3(9), 965–989.

483 Liu, Q., Wen, N., & Liu, Z. (2006). An observational study of the impact of the North Pacific SST
484 on the atmosphere. *Geophysical Research Letters*, 33(18).

485 Liu, Z., & Wu, L. (2004). Atmospheric Response to North Pacific SST: The Role of Ocean–
486 Atmosphere Coupling. *Journal of Climate*, 17(9), 1859–1882.

487 Lorenzo, E. D., & Mantua, N. (2016). Multi-year persistence of the 2014/15 North Pacific marine
488 heatwave. *Nature Climate Change*, 6(11), 1042–1047.

489 Ma, X., Chang, P., Saravanan, R., Montuoro, R., Hsieh, J.-S., Wu, D., Lin, X., Wu, L., & Jing, Z.
490 (2015). Distant Influence of Kuroshio Eddies on North Pacific Weather Patterns? *Scientific*
491 *Reports*, 5(1), 17785. <https://doi.org/10.1038/srep17785>

492 Mills, K. E., Pershing, A. J., Brown, C. J., Chen, Y., Chiang, F.-S., Holland, D. S., Lehuta, S., Nye, J.
493 A., Sun, J. C., & Thomas, A. C. (2013). Fisheries management in a changing climate: Lessons from
494 the 2012 ocean heat wave in the Northwest Atlantic. *Oceanography*, 26(2), 191–195.

495 Namias, J., & Cayan, D. R. (1981). Large-scale air-sea interactions and short-period climatic
496 fluctuations. *Science*, 214(4523), 869–876.

497 Nonaka, M., Nakamura, H., Tanimoto, Y., Kagimoto, T., & Sasaki, H. (2006). Decadal Variability
498 in the Kuroshio–Oyashio Extension Simulated in an Eddy-Resolving OGCM. *Journal of Climate*,
499 19(10), 1970–1989. <https://doi.org/10.1175/JCLI3793.1>

500 Omrani, N.-E., Ogawa, F., Nakamura, H., Keenlyside, N., Lubis, S. W., & Matthes, K. (2019). Key
501 Role of the Ocean Western Boundary currents in shaping the Northern Hemisphere climate.
502 *Scientific Reports*, 9(1), 3014. <https://doi.org/10.1038/s41598-019-39392-y>

503 O’Reilly, C. H., & Czaja, A. (2015). The response of the Pacific storm track and atmospheric
504 circulation to Kuroshio Extension variability: Response of Storm Tracks to Kuroshio Extension
505 Variability. *Quarterly Journal of the Royal Meteorological Society*, 141(686), 52–66.
506 <https://doi.org/10.1002/qj.2334>

507 Putrasahan, D. A., Miller, A. J., & Seo, H. (2013). Isolating mesoscale coupled ocean–
508 atmosphere interactions in the Kuroshio Extension region. *Dynamics of Atmospheres and*
509 *Oceans*, 63, 60–78. <https://doi.org/10.1016/j.dynatmoce.2013.04.001>

510 Qiu, B. (2002). The Kuroshio Extension System: Its Large-Scale Variability and Role in the
511 Midlatitude Ocean-Atmosphere Interaction. *Journal of Oceanography*, 58(1), 57–75.
512 <https://doi.org/10.1023/A:1015824717293>

513 Qiu, B. (2003). Kuroshio Extension Variability and Forcing of the Pacific Decadal Oscillations:
514 Responses and Potential Feedback. *Journal of Physical Oceanography*, 33(12), 2465–2482.
515 <https://doi.org/10.1175/2459.1>

516 Qiu, B., & Chen, S. (2005). Variability of the Kuroshio Extension jet, recirculation gyre, and
517 mesoscale eddies on decadal time scales. *Journal of Physical Oceanography*, 35, 2090–2103.

518 Qiu, B., Chen, S., Schneider, N., & Taguchi, B. (2014). A Coupled Decadal Prediction of the
519 Dynamic State of the Kuroshio Extension System. *Journal of Climate*, 27(4), 1751–1764.
520 <https://doi.org/10.1175/JCLI-D-13-00318.1>

521 Qiu, B., Schneider, N., & Chen, S. (2007). Coupled Decadal Variability in the North Pacific: An
522 Observationally Constrained Idealized Model*. *Journal of Climate*, 20(14), 3602–3620.
523 <https://doi.org/10.1175/JCLI4190.1>

524 Schneider, N., & Cornuelle, B. D. (2005). The Forcing of the Pacific Decadal Oscillation. *Journal*
525 *of Climate*, 18(21), 4355–4373. <https://doi.org/10.1175/JCLI3527.1>

526 Shutts, G. J. (1987). Some comments on the concept of thermal forcing. *Quarterly Journal of the*
527 *Royal Meteorological Society*, 113(478), 1387–1394.

528 Singh, D., Swain, D. L., Mankin, J. S., Horton, D. E., Thomas, L. N., Rajaratnam, B., & Diffenbaugh,
529 N. S. (2016). Recent amplification of the North American winter temperature dipole. *Journal of*
530 *Geophysical Research: Atmospheres*, 121(17), 9911–9928.
531 <https://doi.org/10.1002/2016JD025116>

532 Siqueira, L., Kirtman, B. P., & Laurindo, L. C. (2021). Forecasting remote atmospheric responses
533 to decadal Kuroshio stability transitions. *Journal of Climate*, 34(1), 379–395.

534 Smirnov, D., Newman, M., Alexander, M. A., Kwon, Y.-O., & Frankignoul, C. (2015). Investigating
535 the local atmospheric response to a realistic shift in the Oyashio sea surface temperature front.
536 *Journal of Climate*, 28(3), 1126–1147.

537 Smith, T. M., Reynolds, R. W., Peterson, T. C., & Lawrimore, J. (2008). Improvements to NOAA's
538 Historical Merged Land-Ocean Surface Temperature Analysis (1880–2006). *Journal of Climate*,
539 21(10), 2283–2296. <https://doi.org/10.1175/2007JCLI2100.1>

540 Stevenson, S., Timmermann, A., Chikamoto, Y., Langford, S., & DiNezio, P. (2015). Stochastically
541 Generated North American Megadroughts. *Journal of Climate*, 28(5), 1865–1880.
542 <https://doi.org/10.1175/JCLI-D-13-00689.1>

543 Sugimoto, S., & Hanawa, K. (2011). Roles of SST Anomalies on the Wintertime Turbulent Heat
544 Fluxes in the Kuroshio–Oyashio Confluence Region: Influences of Warm Eddies Detached from
545 the Kuroshio Extension. *Journal of Climate*, 24(24), 6551–6561.
546 <https://doi.org/10.1175/2011JCLI4023.1>

547 Taguchi, B., Nakamura, H., Nonaka, M., Komori, N., Kuwano-Yoshida, A., Takaya, K., & Goto, A.
548 (2012). Seasonal evolutions of atmospheric response to decadal SST anomalies in the North
549 Pacific subarctic frontal zone: Observations and a coupled model simulation. *Journal of Climate*,
550 25(1), 111–139.

551 Taguchi, B., Xie, S.-P., Schneider, N., Nonaka, M., Sasaki, H., & Sasai, Y. (2007). Decadal
552 variability of the Kuroshio Extension: Observations and an eddy-resolving model hindcast.
553 *J.Climate*, 20, 2357–2377.

554 Wang, W., Anderson, B. T., Kaufmann, R. K., & Myneni, R. B. (2004). The relation between the
555 North Atlantic Oscillation and SSTs in the North Atlantic basin. *Journal of Climate*, 17(24), 4752–
556 4759.

557 Wen, N., Liu, Z., Liu, Q., & Frankignoul, C. (2010). Observed atmospheric responses to global SST
558 variability modes: A unified assessment using GEFA. *Journal of Climate*, 23(7), 1739–1759.

559 Xue, J., Sun, C., Li, J., Mao, J., Nakamura, H., Miyasaka, T., & Xu, Y. (2018). Divergent Responses
560 of Extratropical Atmospheric Circulation to Interhemispheric Dipolar SST Forcing over the Two
561 Hemispheres in Boreal Winter. *Journal of Climate*, 31(18), 7599–7619.
562 <https://doi.org/10.1175/JCLI-D-17-0817.1>

563 Xue, Y., Smith, T. M., & Reynolds, R. W. (2003). Interdecadal Changes of 30-Yr SST Normals
564 during 1871?2000. *Journal of Climate*, 16(10), 1601–1612. [https://doi.org/10.1175/1520-
565 0442\(2003\)016<1601:ICOYSN>2.0.CO;2](https://doi.org/10.1175/1520-0442(2003)016<1601:ICOYSN>2.0.CO;2)

566 Zhang, C., Liu, H., Li, C., & Lin, P. (2019). Impacts of mesoscale sea surface temperature
567 anomalies on the meridional shift of North Pacific storm track. *International Journal of*
568 *Climatology*, 39(13), 5124–5139. <https://doi.org/10.1002/joc.6130>

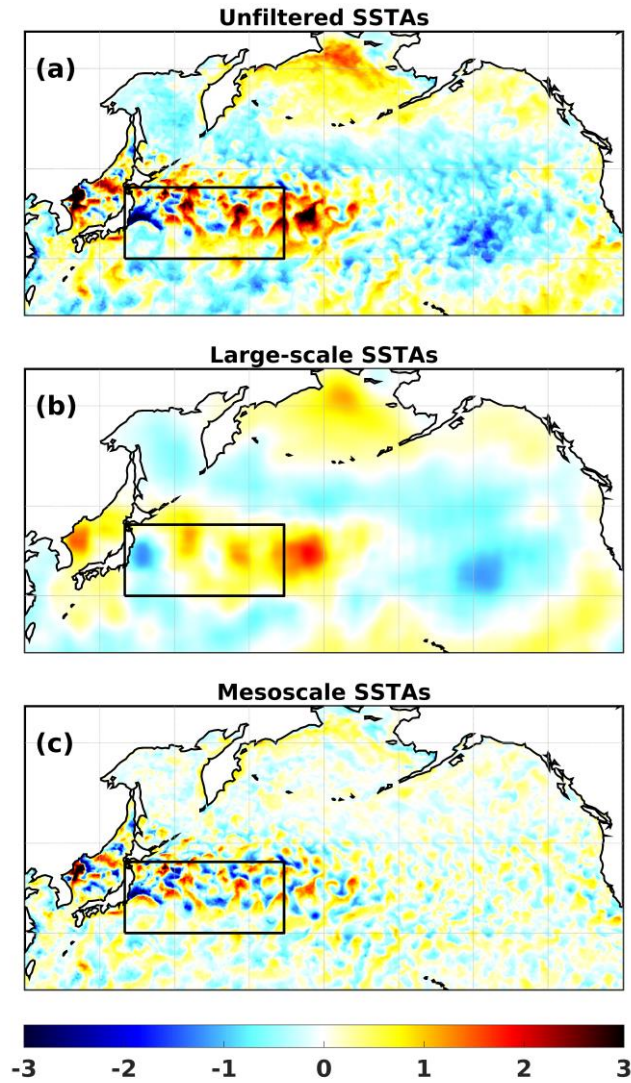
569 Zhou, G., Latif, M., Greatbatch, R. J., & Park, W. (2017). State Dependence of Atmospheric
570 Response to Extratropical North Pacific SST Anomalies. *Journal of Climate*, 30(2), 509–525.
571 <https://doi.org/10.1175/JCLI-D-15-0672.1>

572

573

574

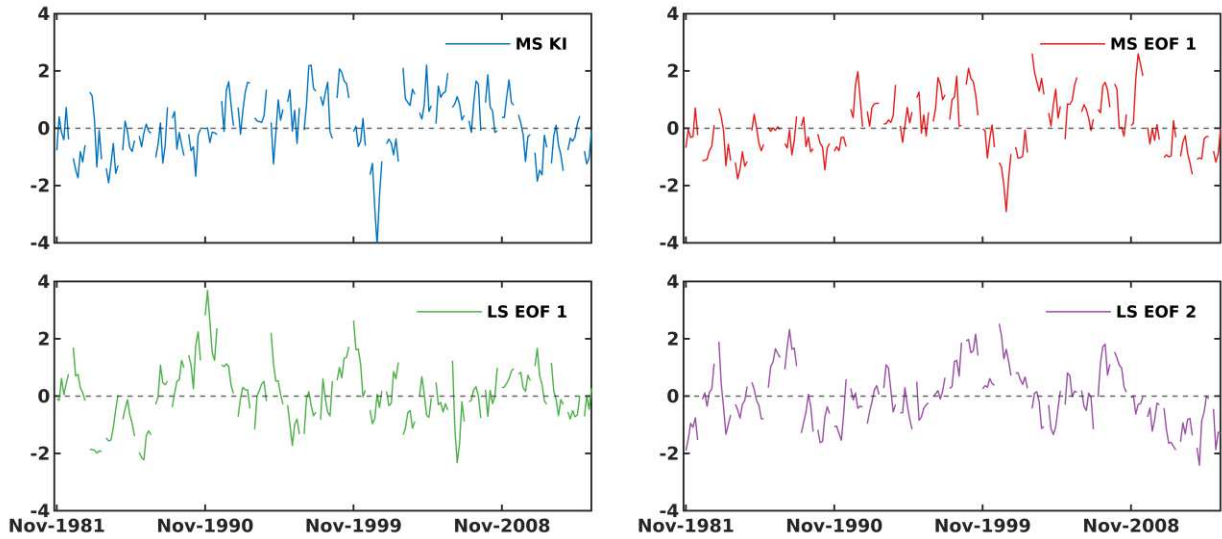
575



577

578 **Fig. 1** Sea surface temperature anomaly (SSTA) signature of (a) Unfiltered SSTAs,
 579 (b) Large-scale SSTAs obtained by applying a 5° x 5° spatial boxcar filter to the
 580 unfiltered SSTAs, and (c) Mesoscale SSTAs obtained by subtracting the Large-scale
 581 SSTAs from the Unfiltered SSTAs. Shading: monthly average SSTA in degrees
 582 Kelvin for December 2003, relative to the climatological mean for period 1981-
 583 2018. Black rectangle: Domain for Kuroshio Extension (KE) region used
 584 throughout this paper.

585



586

587 **Fig. 2** Mesoscale (a,b) and Large-scale (c,d) Kuroshio Extension (KE) indices. (a)
 588 Mesoscale (MS) index obtained using equation 1 from text, applied over KE
 589 domain shown in Fig.1. (b) Leading EOF of MS SSTAs in the KE domain. (c) Leading
 590 EOF for large-scale (LS) SSTAs in the KE domain. (d) Second EOF for LS SSTAs in the
 591 KE domain. All the indices calculated using monthly SSTAs during the Northern
 592 Hemisphere cold season (Nov-Apr).

593

594

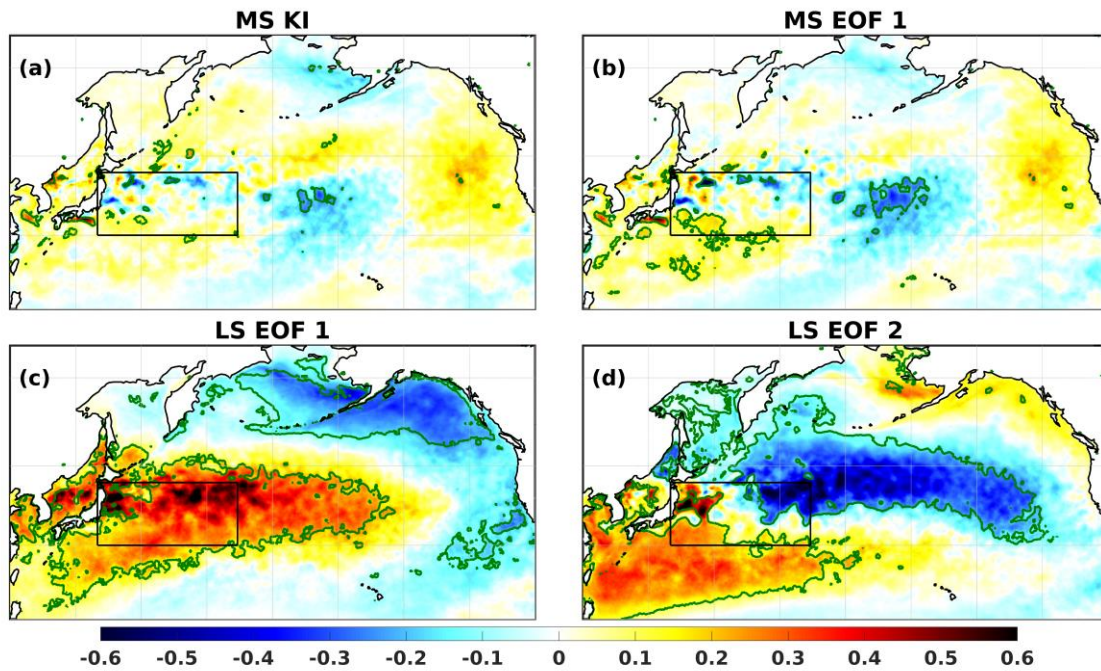
595

596

597

598

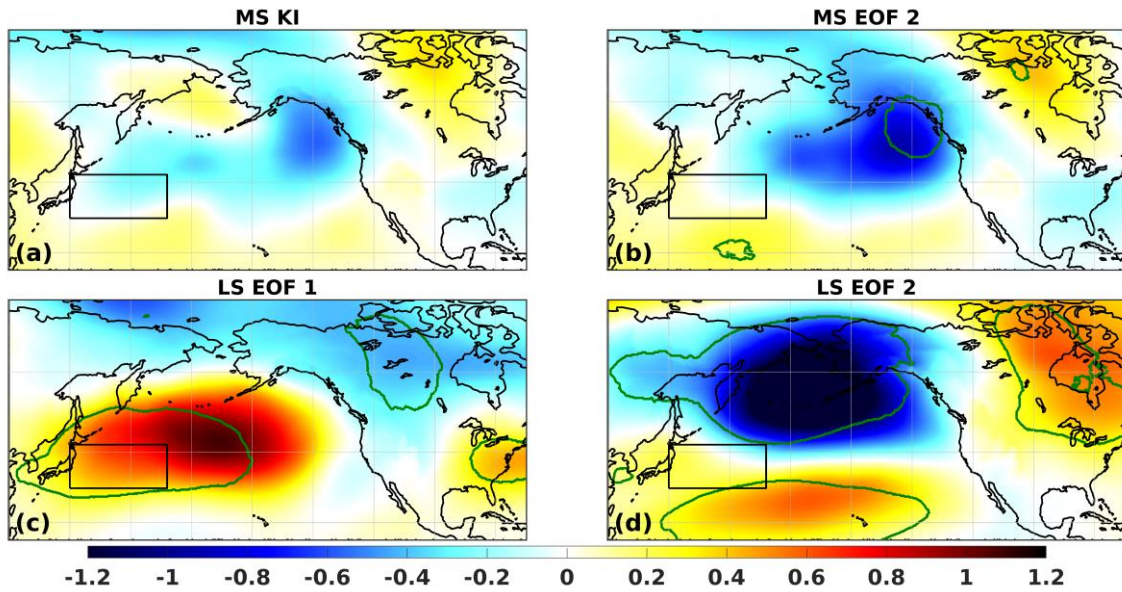
599



601

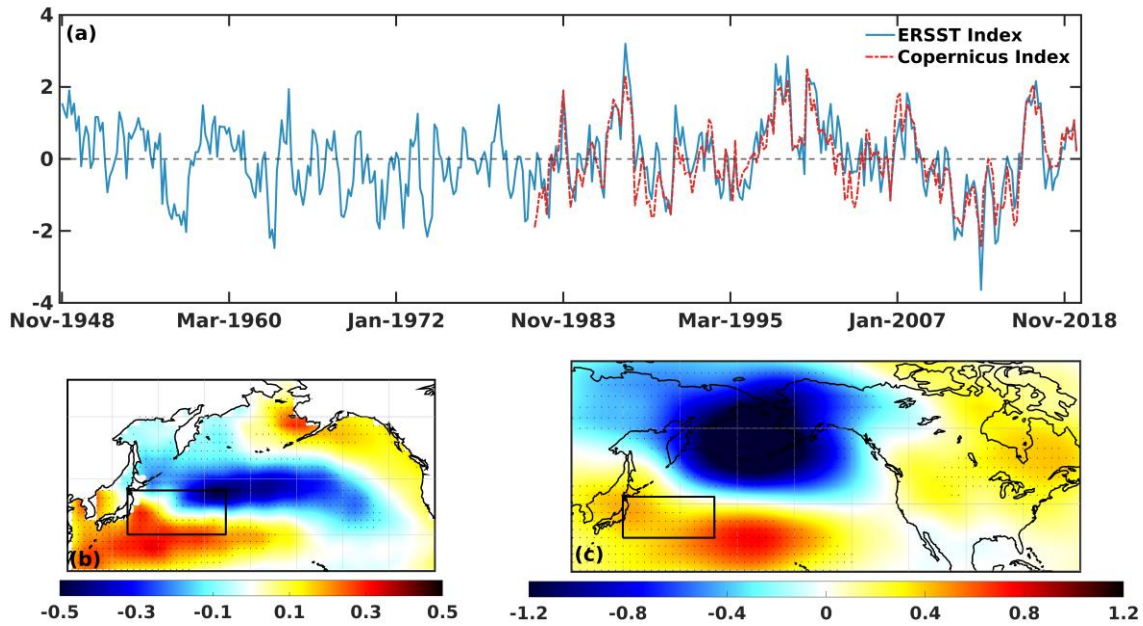
602 **Fig. 3** (a-d) Shading: zero lag regression coefficients of seasonal mean Nov-Apr
 603 SSTAs onto seasonal mean values of (a) MS KI, (b) MS EOF 1, (c) LS EOF 1, and (d)
 604 LS EOF 2 indices. SSTAs (K) are designated by the color bar at the bottom of the
 605 figure. Black rectangle: KE domain. Green contours designate regression
 606 coefficients that exceed the $p < 0.05$ value – see text.

607
608
609
610



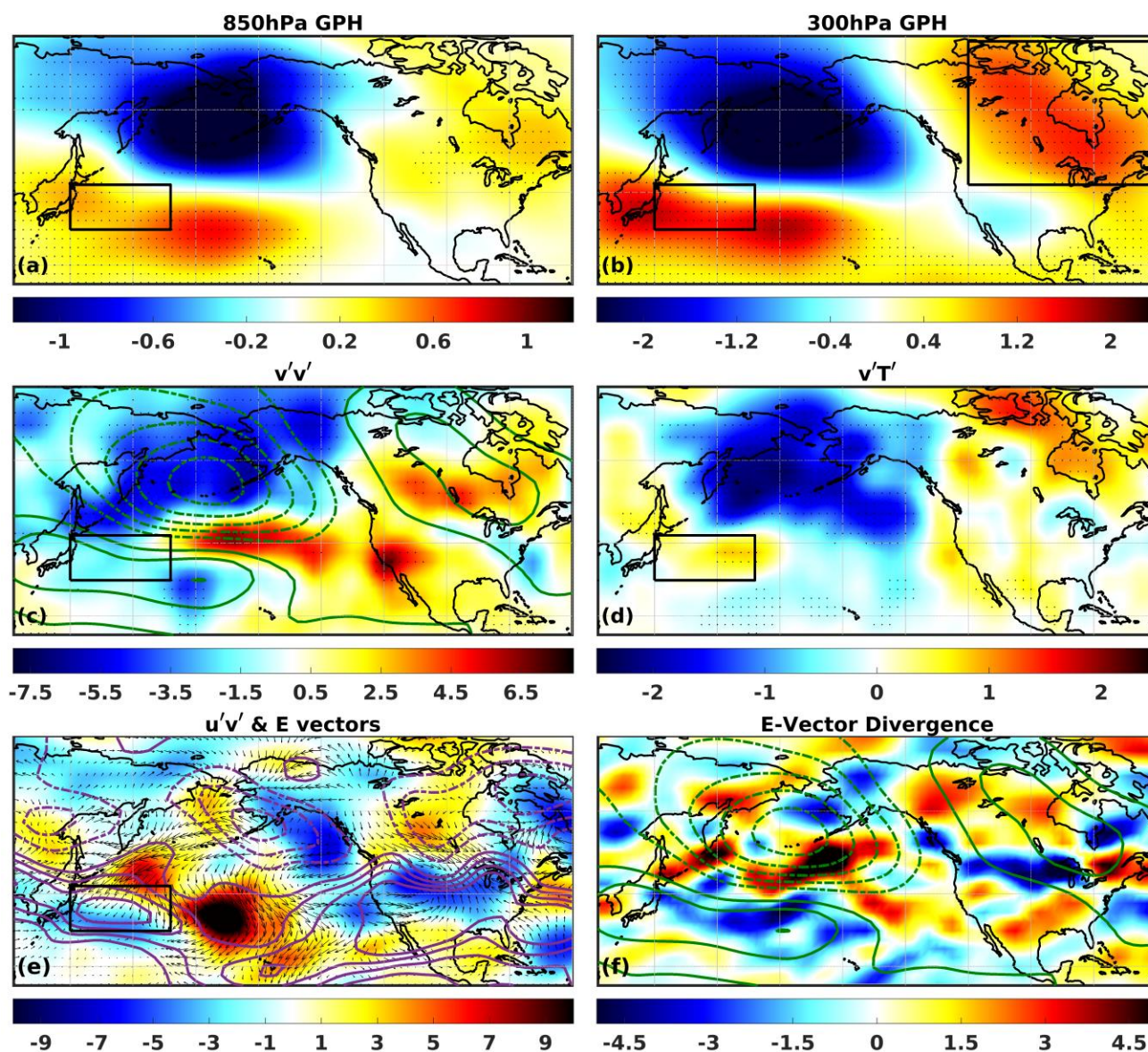
611
612
613
614
615
616
617
618
619

Fig. 4 (a-d) Shading: zero lag regression coefficients of seasonal mean Nov-Apr 850-hPa geopotential height anomalies (GPHAs) onto seasonal mean values of (a) MS KI, (b) MS EOF 1, (c) LS EOF 1, and (d) LS EOF 2 indices. GPHAs (m) are designated by the color bar at the bottom of the figure. Black rectangle: KE region domain. Green contours designate regression coefficients that exceed the $p < 0.05$ value – see text.



620

621 **Fig. 5** (a) A comparison between extended large-scale (LS) EOF 2 time series
 622 generated using low-resolution ERSST data (blue) and LS EOF 2 time series
 623 generated using filtered high-resolution Copernicus data (red). Both indices were
 624 calculated using monthly SSTAs during the Northern Hemisphere cold season
 625 (Nov-Apr). (b) zero lag regression coefficients of seasonal mean Nov-Apr SSTAs
 626 onto seasonal mean values of extended LS EOF 2 time series (shading – Units: K).
 627 (c) zero lag regression coefficients of seasonal mean Nov-Apr 850-hPa
 628 geopotential height anomalies (GPHAs) onto seasonal mean values of extended LS
 629 EOF 2 time series (shading – Units: m). Dotted shading designate regression
 630 coefficients that exceed the $p < 0.05$ value – see text.

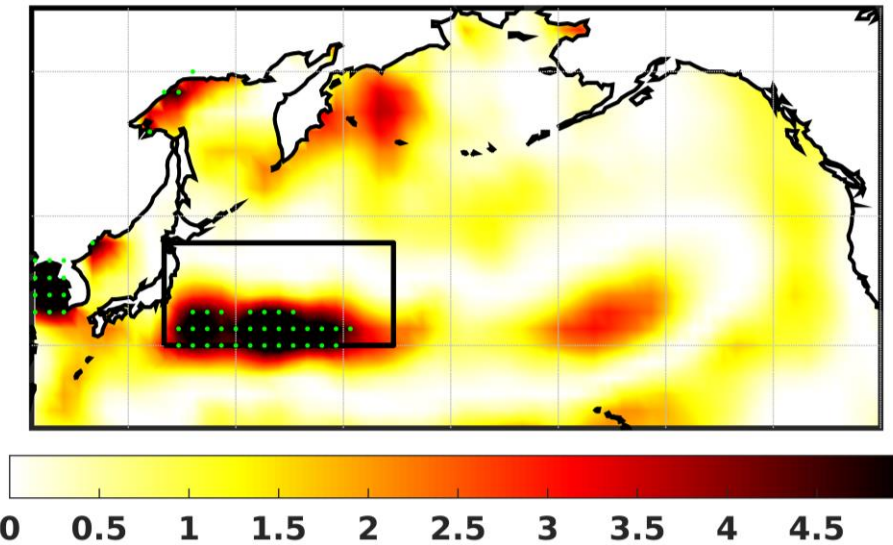


631

632 **Fig. 6** Zero lag regression coefficients of seasonal mean Nov-Apr extended LS EOF
 633 2 time series onto (a) seasonal mean 850hPa geopotential height anomalies
 634 (GPHAs, shading – units: m), (b) 300hPa GPHAs (shading – units: m), (c) 300hPa
 635 storm track activity ($v'v'$) (shading – units m^2s^{-2}) along with 300hPa GPHAs (green
 636 contours), (d) 850hPa meridional eddy heat flux ($v'T'$) (shading – units: Kms^{-1}), (e)
 637 300hPa meridional eddy flux of westerly momentum ($u'v'$) (shading – units m^2s^{-2})
 638 and E-vectors (arrows – units m^2s^{-2}) along with 300hPa $u'v'$ climatology (purple
 639 contours), and (f) Divergence of E-vectors (shading - ms^{-2}) along with 300hPa

640 GPHAs (green contours). Dotted shading designates regression coefficients that
641 exceed the $p < 0.05$ value – see text. Black box domain indicated over North
642 America in figure 6b is the domain that used to construct the monopole index –
643 see text.

644



645

646

647 **Fig.7** Granger causality analysis of early winter (Nov.-Dec.) SST anomalies on the
648 late winter (Jan.-Feb.) Monopole Index (MPI), which represents 300hPa variations
649 over North America – see text for details. Shading is the ω statistic. Green dots
650 indicate ω values that exceed the $p < 0.05$ threshold.

651

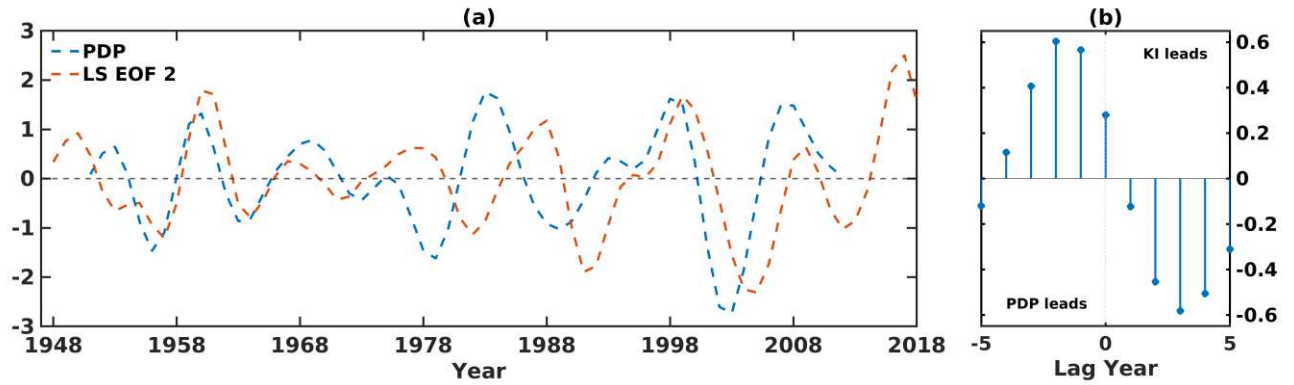
652

653

654

655

656



657

658 **Fig.8** (a) Comparison between 7-20 yr⁻¹ Butterworth bandpass filtered seasonal
 659 mean Nov-Apr KE index, as represented by the extended LS EOF 2 time series, and
 660 the Pacific Decadal Precession (PDP) index, as derived in Anderson et al. (2017).
 661 (b) Lead-lag correlation between the PDP and KE indices.

662

663

664

665

666

667

668

669

670

671